Powder Technology 360 (2020) 241–252

Contents lists available at ScienceDirect

Powder Technology

journal homepage: www.elsevier.com/locate/powtec

Particle tracking velocimetry of porous sphere settling under gravity: Preparation of the model porous particle and measurement of drag coefficients

Likun Ma [a, d], Shuliang Xu [a], Xue Li [b], Qiang Guo [a, c, d], Deyang Gao [b, d], Ya Ding [c, d], Mao Ye [a, c, *], Zhongmin Liu [a, c]

[a] Dalian National Laboratory for Clean Energy, National Engineering Laboratory for MTO, Dalian Institute of Chemical Physics, Chinese Academy of Sciences, Dalian, 116023, China
[b] State Key Laboratory of Catalysis, Dalian Institute of Chemical Physics, Chinese Academy of Sciences, Dalian, 116023, PR China
[c] Dalian National Laboratory for Clean Energy, Division of Energy Environmental Engineering, Dalian Institute of Chemical Physics, Chinese Academy of Sciences, Dalian, 116023, PR China
[d] University of Chinese Academy of Sciences, Beijing, 100049, China

ARTICLE INFO

Article history:
Received 16 November 2018
Received in revised form
14 July 2019
Accepted 18 September 2019
Available online 7 October 2019

Keywords:
Porous sphere
PTV
Terminal velocity
Drag coefficients

ABSTRACT

Porous particles are widely used in liquid–solid and gas-liquid-solid reactors, and accurate prediction of drag coefficients (C_D) for porous particles is essential for designing and optimizing these reactors. The drag coefficients for porous particles, however, have been mainly obtained via theoretical analysis and numerical simulations. Only three experimental studies were carried out to study the drag force on porous spherical particles due to the difficulties in the preparation of model porous spheres with a homogeneous porosity and homogeneous surface properties. In this paper, a method to prepare model porous spheres which have a homogeneous porosity and homogeneous surface properties with a good sphericity for a wider range of relative permeability β has been presented. The details of this method were documented, and it showed that the porous spheres constructed could withstand rigid collisions at the maximum terminal velocity of 1 m/s and keep the structure intact with a negligible quantity of binders. Then gravity-driven settling experiments of a single porous sphere by use of particle tracking velocimetry (PTV) method were carried out to evaluate the feasibility of the use of the prepared porous spheres. Experimental results for 12 porous spheres, with particle Reynolds number (Re) ranging from 1 to 108 and relative permeability β from 21.6 to 315.6, agreed well with the previous results in the literature. The porous particles prepared by our proposed method can be potentially used for measuring drag coefficients of the porous permeable spheres in a wider range of particle Reynolds number and permeability and studying the complex interaction between the porous particles and the surrounding fluid.

1. Introduction

The motion of a permeable particle or a group of sub-particles is widely seen in many industrial and natural processes, including sedimentation of clusters in liquid-solid fluidized bed reactors, motion of coal particles in power stations, transport of porous microcarriers in bioreactors and settling of suspended sediment in coastal waters [1,2]. The drag coefficients of the above porous bodies are crucial in controlling the above processes [3]. And two most typical applications of porous particles in chemical engineering are the porous catalysts in gas-liquid-solid reactors and the particle aggregated 'flocs' in liquid-solid reactors [2,4,5]. Accurate prediction of drag coefficients for porous particles is essential for modeling and optimizing these reactors. The drag coefficients for porous particles, however, have been mainly obtained via theoretical analysis and numerical simulations. Early work mainly focused on theoretical analysis for permeable spheres at very low Reynolds number, in which either Darcy's or Brinkman's equation was used to describe the internal flow of porous particles, and Naiver-Stokes equations were used to solve the surrounding exterior flow. Joseph and Tao [6] showed that the effect of permeability of a spherical porous particle on the drag force was equivalent to

* Corresponding author.
E-mail address: maoye@dicp.ac.cn (M. Ye).

https://doi.org/10.1016/j.powtec.2019.09.058
0032-5910/

the change in the particle radius. Neale et al. [7] derived an analytical solution of the settling velocity of a permeable sphere in creeping flow. Later on, Nandakumar and Masliyah [8] studied the influence of sphere porosity on the drag force, and Padmavathi et al. [9] calculated drag force acting on porous spheres based on an exact solution of a general non-axisymmetric Stokes flow past a stationary porous sphere. Vainshtein et al. [10] showed that, at a low *Re*, the drag force acting on a permeable sphere was smaller than that on an impermeable sphere with the same particle diameter. Although the theoretical analysis presents a robust way to calculate drag force acting on porous particles, it can only be used at low Reynolds number regime (usually $Re \leq 1$) [11–13] where the inertial effect can be neglected and the linear theory is valid.

If the inertial effect cannot be ignored, deriving an analytical solution of drag coefficients C_D for porous particles is quite challenging. In this regard, numerical simulations have been frequently used to study the drag force on porous particles with higher *Re*. Wu and Lee [14] computed the drag force exerted on a permeable sphere for *Re* ranging from 0.1 to 40 by use of CFD software FIDAP 7.5 and found the drag significantly reduced as the porous sphere's permeability became less than some critical value of the normalized radius β of porous spheres. Jain [15] simulated the flow past a porous permeable sphere using FLUENT for a wider range of *Re*, and observed that, the C_D of the porous permeable sphere in the intermediate range of permeability and Reynolds number was greater than that of the impermeable sphere which may be attributed to the formation of circulating cells and back flow inside the porous permeable sphere and as expected, the C_D for the porous sphere with a high *Da* value or a higher Reynolds number is less than that for the impermeable sphere. Yu [2] computed the results of C_D on a porous sphere for *Re* varying from 5 to 100 and found the porous–fluid interface condition may affect the drag acted on the surface of the porous sphere. Wittig [16] also simulated the fluid flow past and through a porous spherical particle over a wide range of *Re* ($20 < Re < 500$) corresponding to different values of porosity varying between 0.62 and 0.92, and found that for a constant *Re* ($Re < 100$), the value of the C_D decreased slightly with increasing porosity. Later on, Wittig [3] further simulated and derived new formulae for the drag coefficients of porous spheres based on different porosities and the results showed the C_D of the permeable porous sphere was smaller than that of the impermeable sphere at a higher *Re* (with $Re > 33$).

However, the theoretical analysis and numerical simulations discussed above have been seldomly verified by experiments due to the difficulties in the preparation of proper model porous particles. To our best knowledge, only three experimental studies were carried out to study the drag force on porous spherical particles. The earliest study of porous sphere experiments began in 1977, Matsumoto and Suganuma [17] carried out some experiments in the low *Re* regime ($Re < 0.6$) using a model aggregate made of steel wool with β being from 3 to 160. They found that the effect of permeability on the settling velocity as well as C_D of a porous aggregate cannot be neglected at lower β and can be approximately evaluated by Brinkman's extension of Darcy's equation $\Omega = 2\beta^2(1 - (tanh\ \beta/\beta))/(2\beta^2 + 3(1 - (tanh\ \beta/\beta)))$ whose assumptions include the shape of the porous sphere must be spherical and there is no permeability distribution in the direction of the porous sphere's radius. Thus, there were some scatterings and significant bias of its experimental data compared with the Darcy-Brinkman equation, which were attributed to the following uncertainties by him: the porous sphere was no good sphericity due to the non-homogeneous surface with a ratio of the longest diameter to the shortest one being about 1.1 and the distribution of porosity within the model aggregate was not homogeneous. Later on, Masliyah and Polikar [4] measured the terminal velocity and thus the C_D of a porous sphere prepared by a semi-rigid plastic foam slab with $15 < \beta < 33$ at *Re* from 0.2 to 120 and its results showed the porous sphere experienced a higher drag than a comparable solid sphere for $7 < Re < 120$ which were different from the common expect that a homogenous porous sphere experienced a lower drag than a comparable solid sphere for both low and high *Re*. The deviation was caused by the sharp increase in the inertial effects on the porous spheres which could be due to a surface effect rather than to internal fluid flow within the porous sphere because the non-homogeneity in the porous medium near the sphere surface was obvious where sharp edges and fiber endings significantly existed. Recently, Emadzadeh [18] carried out the experiments to obtain the terminal velocity and C_D for porous sphere prepared by four alloy wires with different densities for $1 < Re < 10^4$ and clearly pointed out that the porous sphere without a homogeneous distribution of porosity within it could rotate during settlement giving rise to behavior such as the Magnus effect that causes the curving away of the particle from its original falling path. In sum, the homogeneous distribution of porosity within the porous particle and the homogeneous surface properties with a good sphericity [4] cannot be satisfied in all these previous experiments and the pore structures within these previous porous spheres were almost completely uncontrollable. At the same time, they were severely limited to a very small range of particle permeability β.

In this paper, a method has been proposed to prepare model porous particles with a homogeneous porosity and homogeneous surface properties with a good sphericity for a wider range of permeability β. Our model porous particle was modelled as an array of small solid sub-particles and it was itself spherical in shape. To some extent, the pore structures within our model porous spheres were controllable by varying the number of primary spheres, the ratio of primary sphere diameter to the porous sphere diameter and the shape of primary spheres, such as spheres or cubes. The porous spheres constructed in our study could withstand rigid collisions at the maximum terminal velocity of 1 m/s and keep the structure intact with a negligible quantity of binders which were significantly less than that in a similar study in literature [19]. We then evaluated the feasibility of the use of these prepared model porous spheres by particle tracking velocimetry method via gravity-driven settling experiments. We obtained the drag coefficients of our prepared porous spheres with different permeability by use of PTV and compared it with the results in the literature to verify the feasibility of the prepared porous spheres. We will systematically study the interaction between porous particles and the surrounding fluid in our next work. The preparation of model porous spheres and the evaluation of their feasibility are the first step in our series of work. This preparation method is expected to play an important part in the experimental researches related to the flow of porous particles.

2. Materials and methods

2.1. Porous spheres preparation

The new manufacturing procedure of the model porous sphere included three steps: coloring, binding and curing.

2.1.1. Coloring

Glass beads with (nearly) uniform particle size varying from 1 to 6 mm of diameter were selected as primary particles to construct the model porous spheres. As the refractive index of transparent glass beads was similar to that of fluid (i.e. silicone oil in this study), the transparent glass beads cannot be captured clearly by the high-speed camera no matter how to adjust the camera parameters. So, it was desired to color model porous spheres in order to improve the image quality of the high-speed camera in PTV. To this end, the

primary glass beads were first wrapped by an appropriate quantity of unsaturated polyester resin (China Changzhou Huari New Material Co., Ltd. Product Brand: HNH-1001). Then these treated glass beads were roasted under 500 °C in a tube furnace filled up with nitrogen for 30 min. After cooling down, the surfaces of the primary glass beads were evenly deposited with a layer of carbon. The deposition layer was very stable in water, silicone oil or air. The total mass change of the model porous spheres before and after coloring was controlled below 0.8%, as shown in Table 1. The snapshots of the transparent glass beads before and after coloring are shown in Fig. 1.

2.1.2. Binding and Curing

In order to construct the porous spheres, another essential step was binding and curing the primary glass beads together. An organic binding agent, which was also the type of unsaturated polyester resin (China Changzhou Huari New Material Co., Ltd. Product Brand: HNH-1001), was used. This was motivated by the good heat shrinkable properties of this material, which was expected to have a minor effect on the pore structure of the porous spheres. The procedure to construct a porous sphere with the desired diameter was as following. Firstly, a special designed stainless steel mold of a pair of hollow hemispheres with the desired diameter was covered with a release agent (specifically, it was the defilm wax) to avoid the binding agent attachment. Then the primary glass beads were covered with an appropriate quantity of the organic binding agent which was achieved by suction filtration and placed into the stainless steel mold. After many average mixes, the arrangement of the primary glass beads within the stainless steel mold was random accumulation with a homogeneous porosity. After that, the whole mould was put into a furnace, heated at a rate of 5 °C/*min* from room temperature to 150 °C, which was then kept for 36 h, and then cooled at a rate of −5 °C/*min* to room temperature. In this way, the organic binder was evaporated and then solidified to bind the primary glass beads, ensuring the rigidity of the porous sphere.

The total mass ratio of binders in the prepared porous spheres was less than 1.9%, which was 3% in similar study in literature [19] and it was well known that the less binder, the more easily to maximize the real and intrinsic flow of porous spheres which were modelled as an array of small solid primary particles. The detailed data for the total mass ratio of binders was also shown in Table 1. At the same time, the prepared porous spheres could withstand rigid collisions at the maximum terminal velocity of 1 m/s and keep the structure intact with such a negligible quantity of binders. The detailed data of all terminal velocities for porous spheres were listed in Table 5 and the rather good reproducibility of porous spheres under the same experimental condition shown in Fig. 10

Table 1
The total mass change of the tested porous spheres for coloring and binding.

Porous Sphere	Weight change (ΔW_1, %)	Weight change (ΔW_2, %)
#1	−0.07	1.58
#2	−0.07	1.82
#3	0.79	0.09
#4	0.79	0.57
#5	0.17	0.70
#6	0.17	0.56
#7	−0.18	0.85
#8	−0.18	0.92
#9	−0.04	0.63
#10	−0.04	0.47
#11	−0.04	0.62
#12	−0.04	0.65

[1] The data in this Table is the average of three separate weights.
[2] ΔW_1 are the total mass change before and after coloring.
[3] ΔW_2 are the total mass change before and after binding.

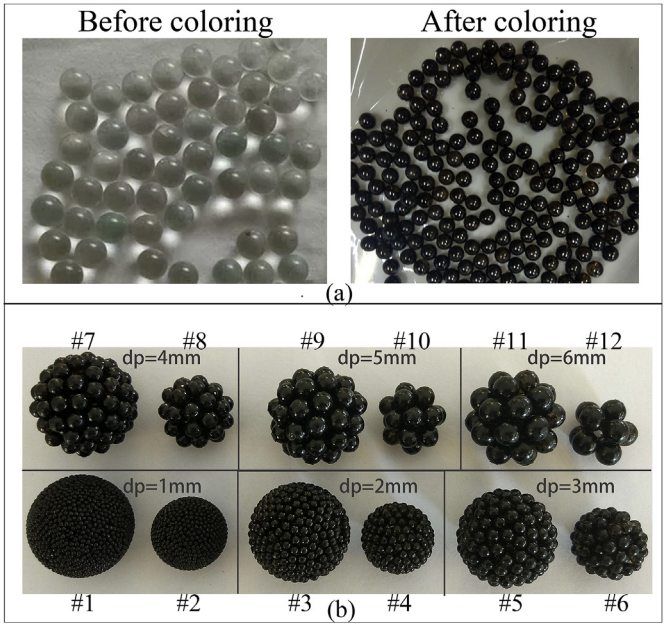

Fig. 1. (a) Primary glass beads before and after coloring. (b) Prepared porous spheres #1-#12: composed of primary glass beads of 1–6 mm.

can also indicate that the prepared porous spheres can sustain the structure under the action of an external force caused by rigid normal impact. The prepared porous spheres, as shown as numbered #1 - #12 in Fig. 1, were correspondingly composed of primary glass beads of 1–6 mm. The specific particle arrangement within the porous sphere after binding was random accumulation after many average mixes and point-to-point contact mode with no coalescence/overlapping of the primary particles with a negligible intermediate connector which was far less than that in a ball-and-stick model porous sphere [20].

2.2. Properties of the porous spheres

In theory, the porosity of a porous sphere composed of evenly distributed primary spheres can be altering by changing the number of primary spheres n and the ratio of primary sphere diameter to the porous sphere diameter d_p/d. The porosity of a porous sphere follows [16]:

$$\varepsilon = 1 - n\sum \mathrm{d_p^3} \Big/ \mathrm{d^3} \tag{1}$$

where d_p is the diameter of the primary sphere, and d is the diameter of the porous sphere prepared. Alternatively, it is also possible to estimate an effective porosity via $\varepsilon_{eff} = 1 - (\rho_{por}/\rho_{gla})$ with ρ_{por} the bulk density of the porous sphere and the ρ_{gla} the density of primary spheres. The results for ε and ε_{eff} in this study shown in Table 2 were very close with a relative error being less than 3% which showed again that the total mass ratio of binders in the prepared porous sphere was rather low, so there was a good preparation effect of our porous spheres with minimal binders which could be safely neglected to maximize the real flow of porous spheres modelled as an array of small sub-particles.

The Darcy number is often used to describe the permeability of a porous sphere:

$$Da = k \Big/ d^2 \tag{2}$$

Table 2
Physical parameters of the tested porous spheres.

Porous Sphere	Monomers Diameter of Glass Beads (d_p, mm)	Porous Sphere Diameter (d, mm)	Monomers Number (n)	Calculated Porosity (ε, %)	Effective Porosity (ε_{eff}, %)	Permeability Coefficient (k, m^2)	Darcy Number (Da, -)	Normalized Sphere Radius (β,-)
#1	1.0	22.8	6695	43.5	42.6	1.3×10^{-9}	2.5×10^{-6}	315.6
#2	1.0	16.8	2836	40.2	39.1	8.9×10^{-10}	3.2×10^{-6}	281.0
#3	2.0	22.8	862	41.8	41.8	4.8×10^{-9}	9.2×10^{-6}	165.0
#4	2.0	16.8	347	41.5	41.1	4.5×10^{-9}	1.6×10^{-5}	125.8
#5	3.0	22.8	252	42.6	42.2	1.1×10^{-8}	2.2×10^{-5}	107.6
#6	3.0	16.8	101	42.5	42.2	1.1×10^{-8}	4.0×10^{-5}	79.4
#7	4.0	22.8	109	41.1	40.6	1.7×10^{-8}	3.3×10^{-5}	87.6
#8	4.0	16.8	43	42.0	41.4	1.8×10^{-8}	6.5×10^{-5}	61.9
#9	5.0	22.8	53	44.1	43.7	3.7×10^{-8}	7.1×10^{-5}	59.5
#10	5.0	16.8	19	49.9	49.7	6.7×10^{-8}	2.4×10^{-4}	32.4
#11	6.0	22.8	27	50.8	50.5	1.0×10^{-7}	2.0×10^{-4}	35.2
#12	6.0	16.8	10	54.4	54.1	1.5×10^{-7}	5.4×10^{-4}	21.6

$$\beta = R \Big/ \sqrt{k} \tag{3}$$

where k is the permeability coefficient, R is the radius of the porous sphere, and β is the normalized radius of the porous sphere which is a very important characteristic parameter to represent the relative value of the permeability. And the permeability coefficient k for the prepared porous sphere is calculated using the Carman-Kozeny relation:

$$k = \left(d_p^2 \varepsilon^3\right) \Big/ \left(180(1-\varepsilon)^2\right) \tag{4}$$

In this work, porous spheres containing different numbers of primary glass beads were constructed following the aforementioned procedure. The physical properties of these porous spheres were summarized in Table 2. Table 2 shows the relative permeability β of the porous spheres has been widened to a wider range $21.6 < \beta < 315.6$ in this study compared with the previous literatures [4,17].

3. Gravity-driven settling of porous spheres by PTV

The primary objective of the PTV experiments is to measure the terminal velocity of the porous spheres. By this way, it is possible to further obtain drag coefficients and compare the results with that in the previous literature, and ultimately verify the feasibility of using the prepared porous spheres in the fluid mechanics study related to permeable particles. Besides, the relative offset of the settling trajectory from the top coordinate position to the bottom coordinate position $\Delta x/\Delta y$ (Δx is the pixel offset in the x-direction and Δy is the pixel offset in the y-direction) for all prepared porous sphere, to some extent, can quantitatively characterize the internal uniformity of the porous sphere because the porous sphere will rotate due to the non-homogeneous within the porous spheres during settlement giving rise to behavior such as the Magnus effect that causes the curving away of the particle from its original falling path [18]. Meanwhile, the sphericity data of the prepared porous sphere can partly reflect the homogeneous surface properties because the sphericity is going to get worse due to the non-homogeneity in the porous medium near the sphere surface where sharp edges and fiber endings significantly exist.

3.1. Experimental setup

The whole process of the settling porous spheres in the viscous fluid from the moment of its release until its rest at the bottom of the vessel was measured. We obtained the trajectory of porous spheres, including the position and the velocity as the function of time, by the high-speed camera via a PTV method. The high-speed camera is equipped with a MEMRECAM HX-3 CMOS sensor, which can reach a maximum of 1,300,000 frames per second and obtain a maximum resolution of 2560×1920 pixels. In this work, the framing rate of 100–1000 frames/s and the shutter time of 5 ms were used. The required illumination was provided by a perpendicularly placed high-power (500 W) Light Emitting Diode (LED). The LED was a cold light source, so it had no effect on the temperature of the fluid in the experiments in order to ensure the viscosity of the fluid was constant.

The initial release position of the porous sphere was below the liquid level to ensure no air in the pores of the porous sphere. In order to release the porous sphere while simultaneously trigger the camera system, an automatic releasing system was designed. The automatic releasing system and PTV were synchronized in the PC, which ensured the experiments can be repeated accurately. The schematic diagram of the experimental apparatus was shown in Fig. 2a. In order to take the wall effect into account, three different rectangle vessels made of plexiglass (5 mm thick) were used, and the dimensions of depth × width × height were $250 \times 250 \times 300$ mm, $200 \times 200 \times 300$ mm and $150 \times 150 \times 300$ mm, respectively, as shown in Fig. 2b.

The fluid used in this study was silicone oil (SHANGHAI RESIN FACTORY CO., LTD) which had good optical accessibility and weak temperature dependency of the viscosity. And three kinds of silicon oil (Silicon Oil 201–100, 201–532, 201–1000) with dynamic viscosity varying from 100 cp to 1000 cp were used to change the Re for the same settling sphere. Though the viscosity of silicon oil only had a weak temperature dependency of the viscosity, we still calibrated the actual dynamic viscosity of three kinds of silicon oil used in our study using a Rheocalc V3.2 Build 47–1 (#1) type viscometer. Table 3 lists the calibrated dynamic viscosity as a function of temperature and we can obtain the value of dynamic viscosity according to the recorded experimental temperature. As can be seen from the viscosity-temperature relationship in Table 3, in all experiments, the fluid can be considered as a Newtonian fluid. And the detailed data of viscosity for impermeable spheres experiments and porous spheres experiments are listed in Table 4 and Table 5, respectively.

The density of silicon oil was measured with specific gravity bottles and the density for three kinds of silicon oil 201–100, 201–532, 201–1000 were respectively 959.940 kg/m^3, 965.484 kg/m^3, and 966.092 kg/m^3.

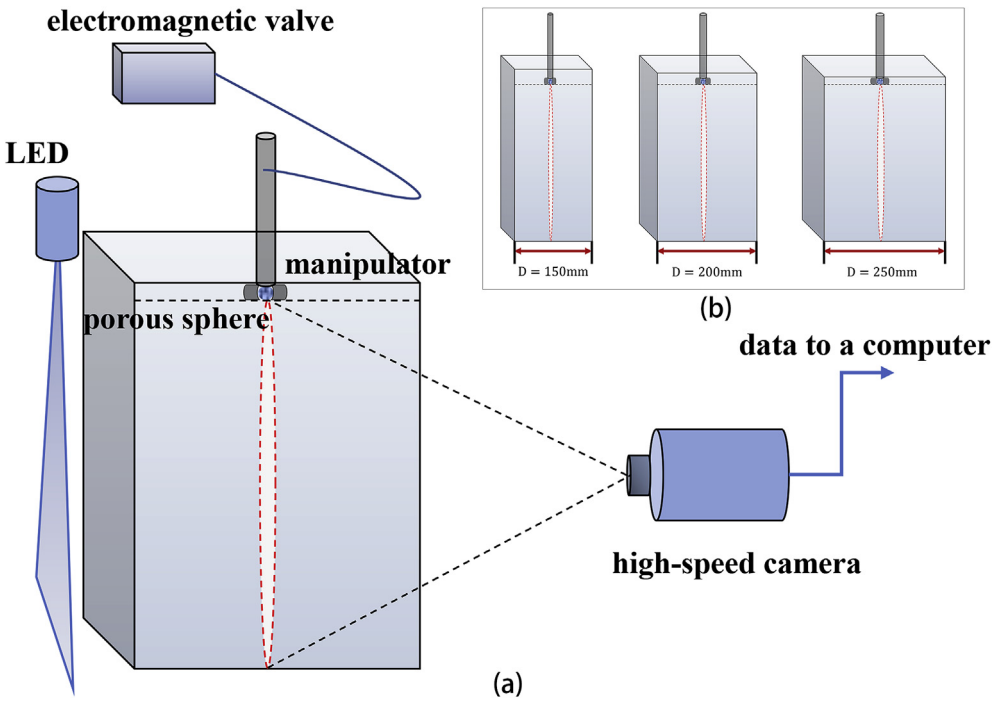

Fig. 2. (a) Experimental setup of PTV system. (b) Three different sizes of rectangle vessels.

Table 3
The calibrated viscosity-temperature relationship for silicon oil.

Silicon Oil	Relationship (μ, cp)[a]	R_{rela}
201−100	$\mu = 171.22684 - 3.83813 \times T + 0.06025 \times T^2 - 6.31902 \times 10^{-4} \times T^3 + 2.28732 \times 10^{-6} \times T^4$	0.99989
201−532	$\mu = 821.88822 - 16.74551 \times T + 0.10367 \times T^2 + 0.0026 \times T^3 - 4.46419 \times 10^{-5} \times T^4$	0.99999
201−1000	$\mu = 1612.651 - 27.80162 \times T - 0.068 \times T^2 + 0.01 \times T^3 - 1.07647 \times 10^{-4} \times T^4$	0.99998

[4] The relationship is about dynamic viscosity μ depending on the temperature T (°C).
[5] The relationship in this Table use polynomial fitting, which is forth order polynomial and R_{rela} is the correlation coefficient of polynomial fitting.

Table 4
Physical parameters and experimental results of the impermeable spheres.

Impermeable Sphere	Sphere Diameter (d, mm)	Sphere Density (ρ_p, g/cm^3)	Viscosity of silicon oil (μ, pa.s)	$Re_t(-)$	u_t (m/s)
#1	10	1.17	0.5261	0.33	0.018
#2	10	1.42	0.5261	0.78	0.042
#3	15	1.16	0.5261	1.06	0.038
#4	20	1.17	0.5261	2.32	0.063
#5	15	1.42	0.5261	2.31	0.084
#6	20	1.42	0.5261	4.78	0.130

3.2. Results and discussion

Instantaneous settling velocities of the tested settling spheres were obtained from settling time and displacement between two adjacent frames measured by a high-speed camera. The formula of the instantaneous velocity is written as Eq. (5):

$$U(t) = s(t) / M\Delta t \tag{5}$$

where $s(t)$ is the displacement between two adjacent frames, Δt is the time between two adjacent frames, M (pixel/mm) is the scaling factor of the high-speed camera and $U(t)$ is the instantaneous settling velocities.

For image identification and quantitative analysis in the data processing, an in-house code was developed. The information quantifying a sphere settling under gravity by PTV was derived from photos via this in-house code, which involved in a sequence of operations as following: (1) extraction of the region of interest, (2) grayscale, (3) binarization, (4) filtration, (5) boundary identification and (6) centroid determination. Then the instantaneous velocity was evaluated using Eq. (5) by measuring the centroid's displacement and the travel time between two adjacent frames of the high-speed camera. The typical photos were illustrated in Fig. 3.

Note that the terminal settling velocity occurs which is also called the steady-state motion when the net gravitational force (gravity minus buoyancy) equals the drag force, as defined in Eq. (6).

$$G - F_b = F_d \tag{6}$$

The net gravitational force $G - F_b$ and the drag force F_d on a sphere are described as in Eqs. (7) and (8):

Table 5
Physical parameters and experimental results of the permeable spheres.

Permeable Sphere	$Re_t(-)$	$C_D(-)$	u_t(m/s)	$\Omega(-)$	$\lvert\Delta x/\Delta y\rvert(\%)$	Sphericity	$S''(-)$
#1	3.6	9.63	0.175	1.06	0.98	0.91	12.88
#2	1.7	17.70	0.114	1.07	1.06	0.91	10.05
#3	3.5	10.04	0.171	1.08	0.76	0.90	6.63
#4	1.8	15.11	0.120	0.97	0.99	0.90	4.92
#5	3.7	8.66	0.181	0.99	0.83	0.89	4.36
#6	1.7	16.36	0.113	0.99	1.01	0.89	3.22
#7	3.8	8.51	0.182	0.98	0.48	0.88	3.35
#8	1.7	15.83	0.114	0.97	1.07	0.88	2.44
#9	3.5	9.35	0.170	1.01	0.77	0.88	2.55
#10	1.6	15.97	0.106	0.92	0.54	0.86	1.68
#11	3.3	9.01	0.160	0.94	0.53	0.85	1.87
#12	1.5	16.45	0.098	0.89	1.24	0.85	1.28
#1	11.3	4.06	0.270	1.03	0.70	0.91	12.88
#2	5.7	6.69	0.186	1.05	0.85	0.91	10.05
#3	11.3	4.02	0.270	1.02	0.73	0.90	6.63
#4	5.7	6.49	0.184	1.02	0.007	0.90	4.92
#5	11.4	3.83	0.272	0.98	0.92	0.89	4.36
#6	5.6	6.36	0.182	0.99	0.60	0.89	3.22
#7	11.3	3.85	0.271	0.98	0.54	0.88	3.35
#8	5.6	6.24	0.182	0.98	0.004	0.88	2.44
#9	11.1	3.84	0.265	0.97	0.003	0.88	2.55
#10	5.2	6.23	0.169	0.94	0.24	0.86	1.68
#11	10.3	3.80	0.246	0.93	1.34	0.85	1.87
#12	4.9	6.19	0.159	0.90	0.31	0.85	1.28
#1	104.6	1.07	0.530	0.99	0.25	0.91	12.88
#2	58.2	1.46	0.400	1.00	0.43	0.91	10.05
#3	101.5	1.12	0.515	1.01	1.95	0.90	6.63
#4	57.5	1.41	0.395	0.97	0.49	0.90	4.92
#5	108.3	0.95	0.549	0.93	1.87	0.89	4.36
#6	56.8	1.38	0.391	0.95	0.07	0.89	3.22
#7	105.6	1.00	0.535	0.95	0.21	0.88	3.35
#8	57.2	1.34	0.394	0.93	3.02	0.88	2.44
#9	104.6	0.97	0.530	0.93	4.42	0.88	2.55
#10	54.4	1.28	0.374	0.89	1.82	0.86	1.68
#11	97.2	0.96	0.493	0.90	3.08	0.85	1.87
#12	53.9	1.15	0.371	0.82	0.33	0.85	1.28

$$G - F_b = \pi\left(\rho_p - \rho_f\right)(1-\varepsilon)gd^3 \Big/ 6 \tag{7}$$

$$F_d = C_D \pi d^2 \rho_f u_t^2 \Big/ 8 \tag{8}$$

where g is the gravitational acceleration and for impermeable spheres $\varepsilon = 0$. Combining the above three formulas, the drag coefficient is

$$C_D = \left(4\left(\rho_p - \rho_f\right)(1-\varepsilon)gd\right) \Big/ \left(3\rho_f u_t^2\right) \tag{9}$$

where *Re* for the terminal state is defined as follows:

$$Re_t = \rho_f u_t d \Big/ \mu \tag{10}$$

with u_t being the terminal velocity of settling particle and $\mu/\ \rho_f$ being the kinematic viscosity of fluid.

3.2.1. Validation of PTV measurement system

Because gravity-driven settling of a single impermeable sphere has already been studied by many researchers and obtained the relatively accurate results for C_D [21–23], in this work, firstly, six impermeable spheres whose physical parameters were listed in Table 4 were used to verify the reliability of the PTV measurement system. The experimental fluid was silicon oil 201–532.

Fig. 4 showed the instantaneous velocities obtained by PTV experiment for six impermeable spheres. As can be seen, the trajectories of 6 impermeable spheres, from the moment of release to the steady-state, and to deceleration and rest at the bottom of the vessel, could be clearly identified. In particular, the steady-state motion in which the terminal velocities could be reached, was captured clearly. We could obtain the value of the terminal velocities u_t from the steady-state motion and then further obtain the Re_t and C_D based the u_t using Eqs. (9) and (10).

In addition, to check the repeatability of the experiments, each condition was repeated three times and the standard deviations of the terminal velocities for impermeable spheres were below 0.02%, indicating a rather good reproducibility, as shown in Fig. 5.

As the experiments were carried out in the finite container instead of infinite fluid and the confinement might cause deviation of the terminal velocity results which was also called the side-wall-effects. The u_t obtained directly from the experiments were all based on different ratios of sphere diameter to the vessel width d/D and therefore the Re_t calculated by the above u_t were also based on different d/D. Thus, the correction for the wall effect was made by plotting the sphere Reynolds number, Re_t, at logarithmic scale against the ratio of sphere diameter to the vessel width, d/D. It was argued that extrapolation of Re_t to $d/D = 0$ using the linear regression of Re_t (at logarithmic scale) vs d/D could obtain Re_t for an infinite fluid [4]. The extrapolated Re_t for the six impermeable spheres are shown in Fig. 6. And then we could finally calculated the u_t for an infinite fluid based on the Re_t for an infinite fluid which were obtained after the correction for the wall effect and the u_t of the impermeable spheres for an infinite fluid are shown in Table 4. Also, the corresponding C_D for an infinite fluid could calculated based the u_t for an infinite fluid.

Nian-Sheng Cheng [22] reviewed fourteen correlations in the literature and proposed a five-parameter correlation for explicitly evaluating drag coefficient of spherical impermeable particles, which read

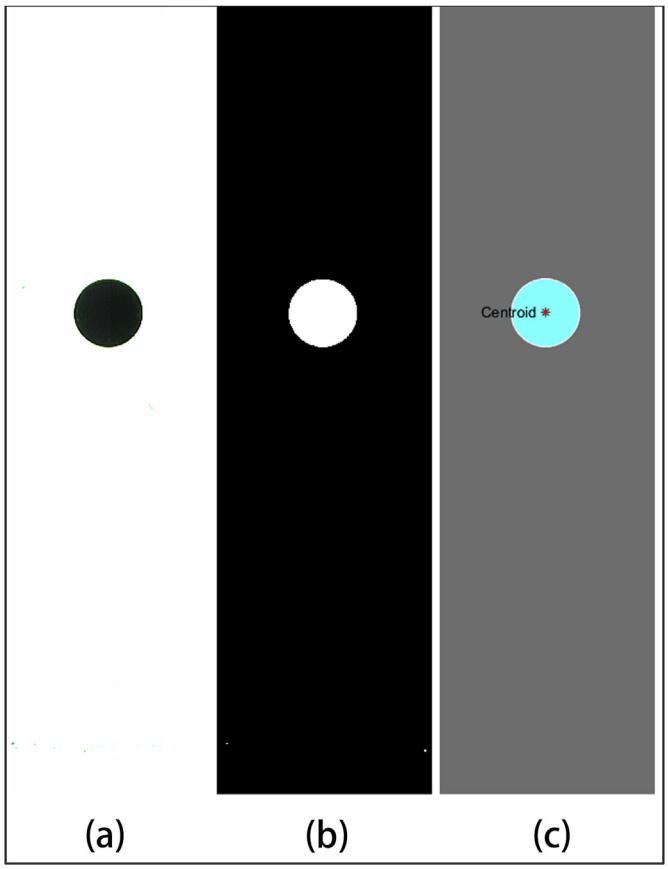

Fig. 3. The image processing procedure for particle settling under gravity: (a) Real sphere, (b) Binarization, (c) Centroid determination.

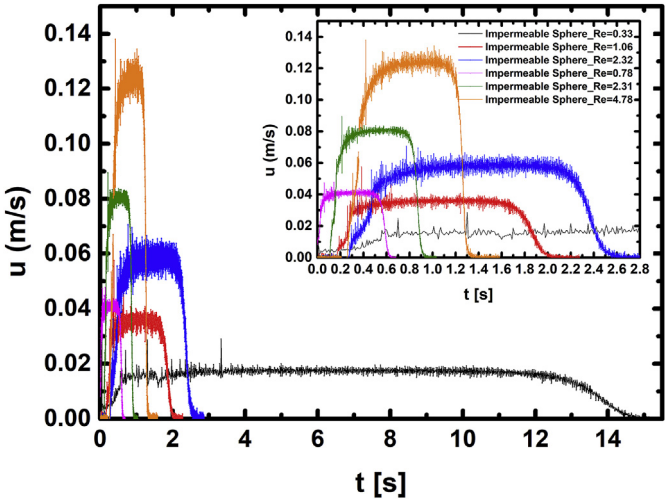

Fig. 4. Instantaneous velocity for six impermeable spheres.

$$C_D = 24(1 + 0.27Re_t)^{0.43} \Big/ Re_t + 0.47\left[1 - exp\left(-0.04Re_t^{0.38}\right)\right] \tag{11}$$

Fig. 7 shows the comparison of our experimental results for impermeable spheres with the correlation by Eq. (11), which shows a good agreement, verifying the reliability of the PTV measurement method in this work.

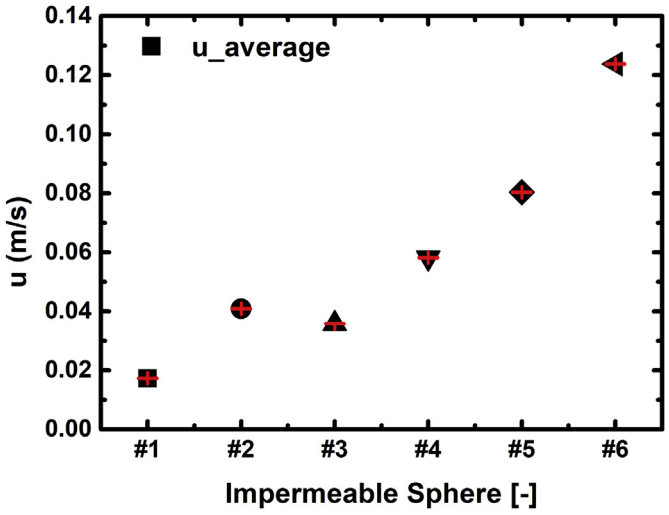

Fig. 5. The error bar of the terminal velocities for six impermeable spheres.

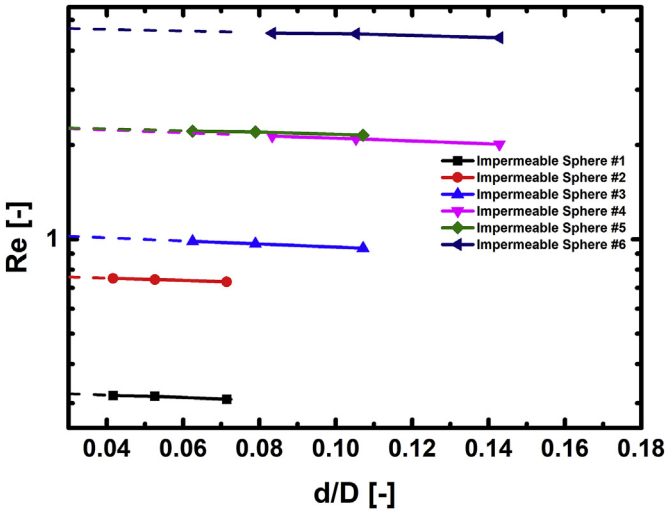

Fig. 6. Reynolds number dependence vs d/D for six impermeable spheres in silicon oil 201-532. (For interpretation of the references to color in this figure legend, the reader is referred to the Web version of this article.)

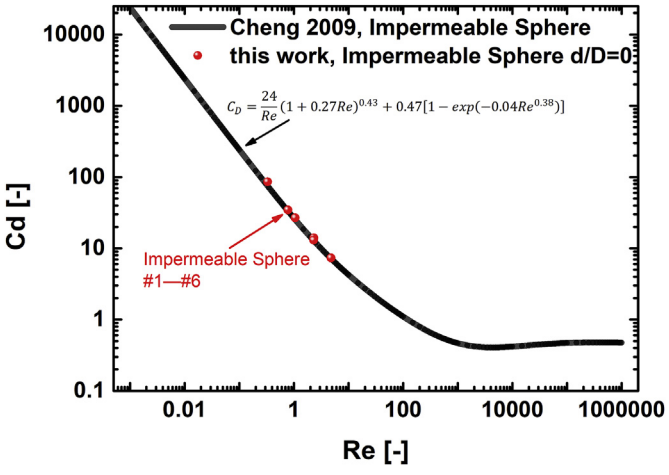

Fig. 7. Six impermeable spheres data and the literature results for $Re - C_D$ correlations.

3.2.2. Experimental results for porous spheres

As mentioned above, in order to evaluate the feasibility of use of this method to prepare model porous spheres in experiments for fluid flow around single porous particle, in total 12 porous spheres were constructed in this work, for which the *Re* was in the range of 1–108 and β varied from 21.6 to 315.6. Three kinds of silicon oil (Silicon Oil 201–100, 201–532, 201–1000) with dynamic viscosity varying from 100 cp to 1000 cp were used to change the *Re* for the same settling sphere. The *Re* of the porous spheres as a function of d/D is shown in Fig. 8 which could obtain the Re_t, u_t and C_D of porous spheres in an infinite fluid. Meanwhile, we can find from Fig. 8 that the wall effects are important for Re_t less than about 5 while the wall effects on the settling velocity are minor for higher *Re*. The slopes of Re_t (at logarithmic scale), as a function of d/D, decrease gradually as *Re* increases, indicating the wall effects become weaker as *Re* increases which is consistent with the previous results in the literature [4]. And it is also found that different β may lead to different wall effects. For porous sphere #10, #11, #12, when $Re_t \approx 2$, as shown in Fig. 9, β are 21.6, 32.4 and 35.2, respectively. The corresponding slopes of ln Re_t vs. d/D are 1.18, 1.22, and 1.34 respectively, indicating the wall effects become more significant with a larger β at a lower Reynolds number, which is also in accordance with the previous porous sphere experimental results [4] indicating the feasibility of the use of the prepared model porous spheres. Note that this work focuses on the preparation and the evaluation of the feasibility of the model porous particle while the study of side-wall-effects is not the main target in this work and the correction for the wall effect is just the intermediate data processing step to obtain the Re_t, u_t and C_D in an infinite fluid. Thus, the detailed correlation between β and the wall effects d/D is not given here which will be systematically study in our next work.

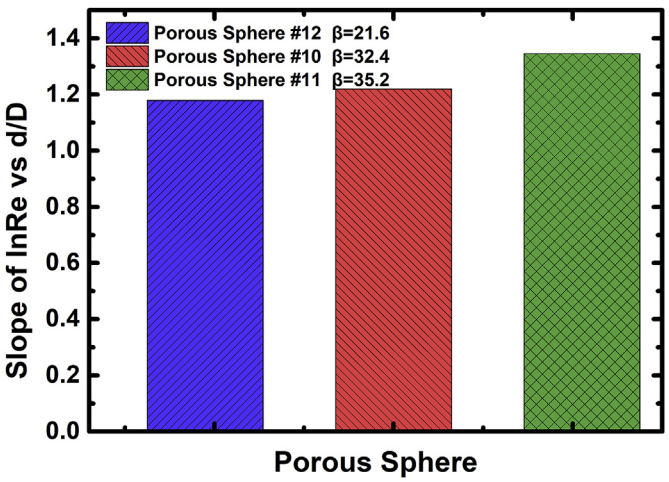

Fig. 9. The wall correction factor dependence on d/D for porous spheres.

The Re_t, u_t and C_D of the porous spheres for an infinite fluid calculated from the extrapolated Reynolds number just as same as

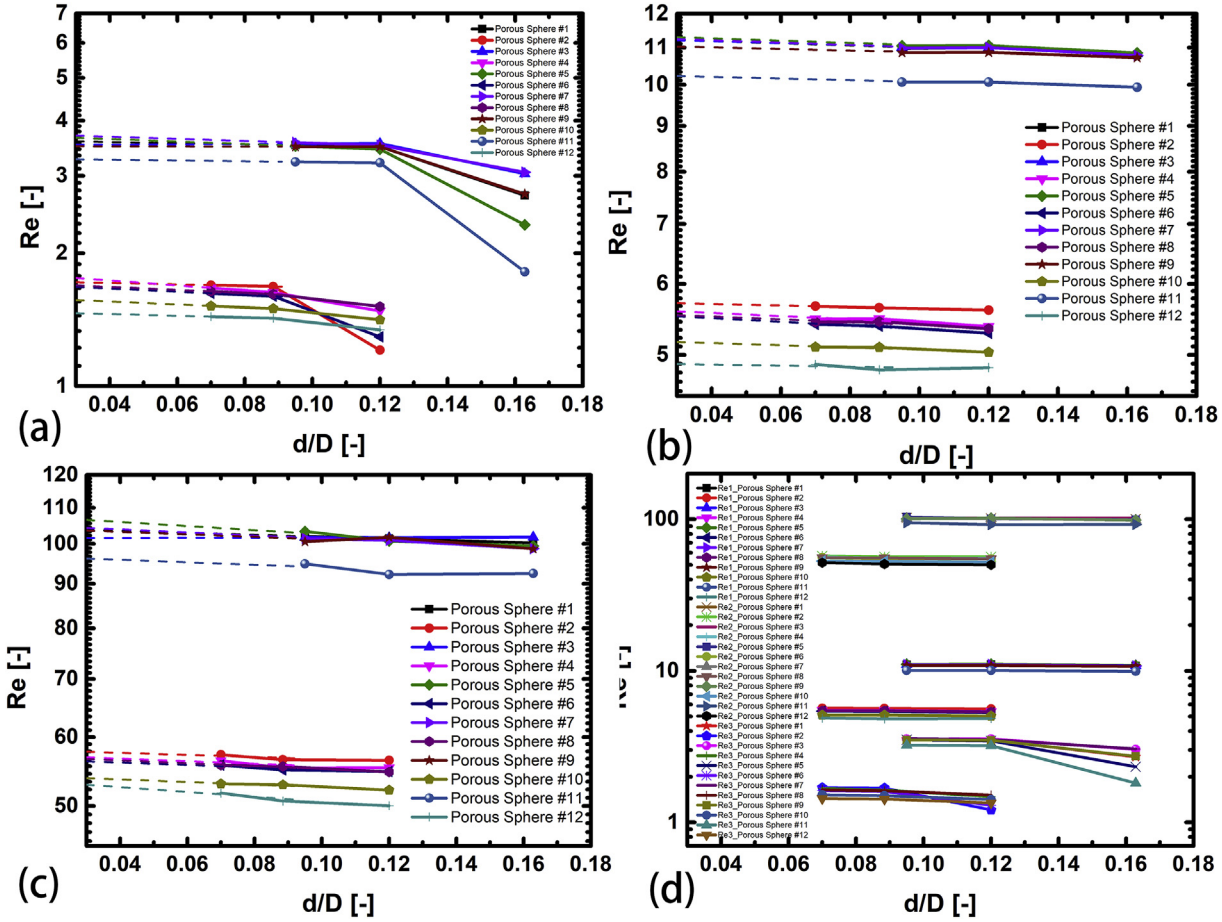

Fig. 8. Reynolds number vs d/D for porous spheres: (a) low *Re* in silicon oil 201–1000, (b) moderate *Re* in silicon oil 201–532, (c) higher *Re* in silicon oil 201–100, (d)summary graphs for all *Re* in silicon oil 201–1000, 201–532, 201–100. (For interpretation of the references to color in this figure legend, the reader is referred to the Web version of this article.)

that for impermeable spheres are shown in Table 5. Besides, the correction factor Ω are also listed in Table 5, which is the most important characteristic parameter for the porous sphere to describe the difference of u_t between porous and non-porous spheres and is defined as $\Omega = drag\ ratio = \frac{drag\ on\ porous\ sphere\ of\ radius\ R\ in\ unbounded\ fluid}{drag\ on\ impermeable\ solid\ sphere\ of\ radius\ R\ in\ unbounded\ fluid} = \frac{u_{t,p}}{u_{t,im}}$ (Note: the porous sphere has the same volume and bulk density ($\rho_{bulk} = \rho_p \cdot V_p + \rho_f \cdot V_f$, including the fluid inside the porous sphere) with the corresponding impermeable spheres). We can see from Table 5 that Ω generally decreases with β decreasing which is consistent with the common perception of porous spheres drag and indicating partly the feasibility of the prepared spheres. However, the detailed relationship between Ω and β has not been present here due to it is not the main target of this work. Besides, the experiments were also repeated three times for each condition, and the standard deviations of the terminal velocities for the porous spheres are typically below 0.2%, also indicating a good reproducibility as shown in Fig. 10. At the same time, the prepared porous spheres underwent a rigid normal impact with the bottom wall of the vessel in each experiment and the maximum terminal velocity in present experiments was 1 m/s shown in Table 5. The force-displacement curves or the breakage curves of porous spheres prepared should be done in our next step to further characterize its strength properties [20]. In all present experiments, the prepared porous spheres could keep the structure intact under the action of an external force caused by the rigid normal impact and presented a rather good reproducibility shown in Fig. 10 with such a negligible quantity of binders which were significantly less than that in a similar study in the literature [19].

Meanwhile, the relative offset of the settling trajectory from the top coordinate position to the bottom coordinate position Δx/Δy (Δx is the pixel offset in the x-direction and Δy is the pixel offset in the y-direction) for all prepared porous sphere were calculated shown in Table 5, to some extent, to quantitatively characterize the internal uniformity of the porous sphere because the porous sphere could rotate during settlement giving rise to behavior such as the Magnus effect that caused the curving away of the particle from its original falling path [18]. And we can see from Table 5 that the relative offsets Δx/Δy of the prepared porous spheres are below 4.5% indicating that the settling trajectories are almost straightforward due to the relatively homogeneous porosity distributions. And as shown in Table 5, the sphericities of the prepared porous spheres are rather good which are above 85% indicating partly the surface properties are relatively homogeneous due to the non-homogeneity in the porous medium near the sphere surface where sharp edges and fiber endings significantly exist will contribute to a bad sphericity. Here, a new parameter S'' which was proposed by Wittig [3] is introduced to describe the surface roughness properties quantitatively to some extent and S'' represents the surface ratio of a porous sphere compared to a solid sphere, defined as $S'' = (nS_p - S_{int})/S_0$ with S_0 the reference surface area of a solid sphere with a diameter d, S_p the surface of a single primary sphere with a diameter d_p, n the number of the primary spheres and S_{int} the overlapping surfaces among the primary spheres (Note: S_{int} is always 0 in our model porous spheres due to the point-to-point contact mode within our prepared porous spheres with no coalescence/overlapping of the primary particles). And in Fig. 11, although there is a slight fluctuation when $Re < 5$ which may be attributed to the experimental data are too few, the dependence of C_D on S'' is proportional to the term $1/\sqrt{S''}$ when $11 < Re < 108$ which is within the scope of the Re and in accordance with the results found by sensitivity analysis in the previous literature [3]. It can also indicate partly the feasibility of the prepared spheres and the deep and quantitative analysis on the surface roughness properties will be done in our next work.

In order to further verify the feasibility of the model porous particle that we prepared, we compared our results of the wall correction factor K and drag coefficient C_D in an infinite fluid

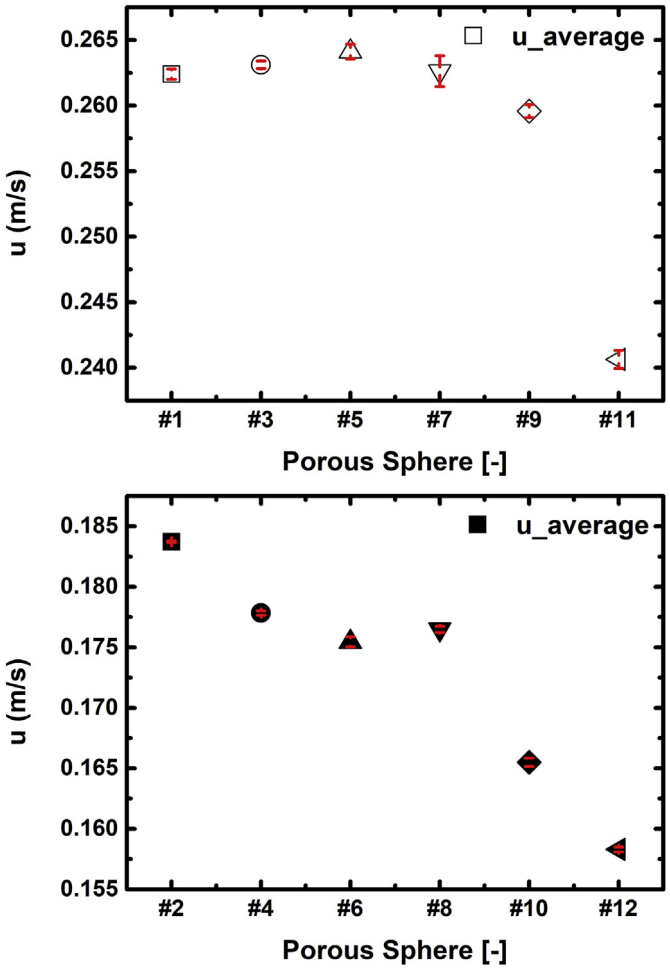

Fig. 10. The error bar of the terminal velocities for porous spheres.

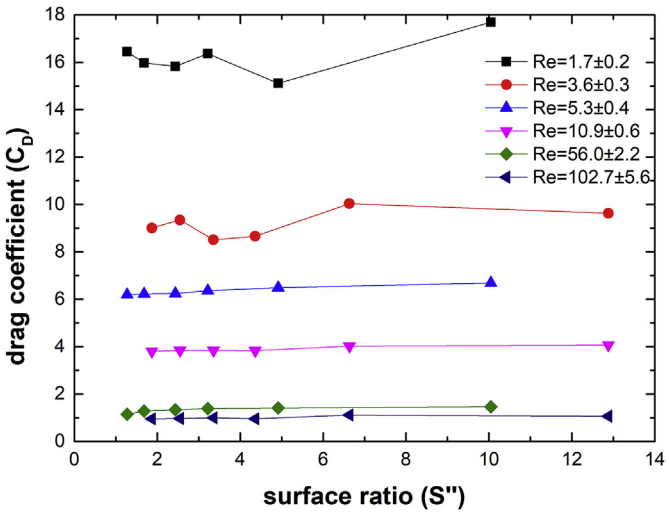

Fig. 11. The dependence of C_D on S'' for porous spheres.

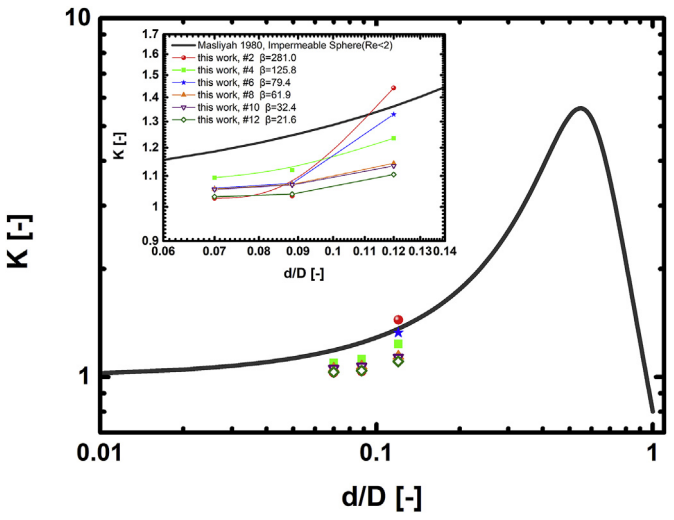

Fig. 12. The wall correction factor dependence on d/D for porous spheres.

without side wall effects with those in the literature [2–4,8,15,16].

Masliyah and Polikar [4] found the wall correction factor K for permeable spheres at $Re < 2$ was very similar to that of impermeable spheres as defined by Eq. (12).

$$K \approx \left[1 - 2.25d/D + 2.5(d/D)^3\right]^{-1} \tag{12}$$

here, d was the diameter of the whole sphere, D was the dimensions of the vessel and $K = Re_{t,\ 0}/Re_{t,\ d/D}$ was the ratio of particle Reynolds number for an infinite fluid ($Re_{t,\ 0}$) and particle Reynolds number for a finite fluid ($Re_{t,\ d/D}$) based on the same sphere. As shown in Fig. 12, when $Re < 2$, there is a good agreement between our results of the wall correction factor K and the predictions by Eq. (12), which also shows the feasibility of the prepared spheres.

Meanwhile, to our best knowledge, based on the particle Reynolds number and permeability, there were two explicit drag coefficient correlations for porous spheres proposed by the previous literatures. Masliyah and Polikar [4] proposed a semi-empirical correlation, which was now widely accepted for $Re - C_D$, by experiments with porous spheres made of semi-rigid plastic foam. The correlation obtained from the experiment [4] was as following Eq. (13) and Eq. (14):

For $0.1 < Re \leq 7$

$$C_D = 24\Omega\left[1 + 0.1315Re^{(0.82-0.05\omega)}\right] / Re \tag{13}$$

For $7 < Re < 120$

$$C_D = 24\Omega\left[1 + 0.0853Re^{(1.093-0.105\omega)}\right] / Re \tag{14}$$

Here β is in the range of 15–33, $\omega = log_{10}Re$, $\Omega = 2\beta^2(1 - (tanh\beta/\beta))/(2\beta^2 + 3(1 - (tanh\beta/\beta)))$.

And Jain [15] obtained the $Re - C_D$ correlation for a porous permeable sphere from the CFD simulation data, which was written as $C_D = [34 - 134(k/d^2) + 208(k/d^2)^2 - 104(k/d^2)^3]Re^{-0.8}$, with $0.1 \leq Re \leq 100$, $0 \leq k/d^2 \leq 1$. Besides, although there was no clear correlation based on the Re and k proposed, Nandakumar, Yu and Wittig [2,3,8,16] also computed the C_D for a porous permeable sphere for specific particle Reynolds number and permeability (or porosity) by numerical simulations.

Fig. 13 shows the plot for the drag coefficient against the particle Reynolds number at different permeability ratio values based on

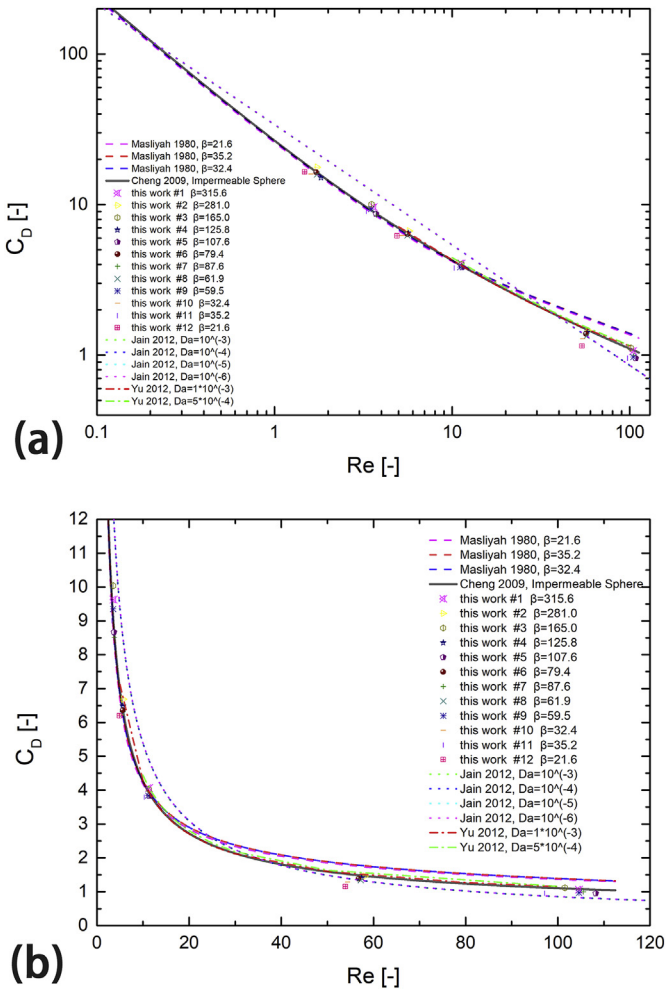

Fig. 13. Comparison of our experimental results with the $Re - C_D$ correlations in the literature: (a) General drawing for the whole experimental range, (b) A partial enlarged drawing for $0 < C_D < 12$

the results in the literature and our experimental data. The black solid line indicates the drag coefficient values for an impermeable sphere [22], whereas different dashed lines and chain lines indicate the drag coefficient for a permeable sphere obtained by different researchers [2,4,15] and the dot represent our porous spheres data. We compared our experimental results with the results in the literatures, as shown in Fig. 13(a) and (b), and the detailed values of our experimental data are shown in Table 5. We can see from Fig. 13 that for $0.1 < Re \leq 7$, the C_D obtained in our experiments with specially constructed porous spheres collapses to one line with the C_D for solid spheres, indicating C_D for homogenous permeable spheres tends to be consistent with that for impermeable spheres with a same Re. This result agrees well with the general results, such as the results of Masliyah [4] and Yu [2]. And for $7 < Re < 108$, our C_D experimental results for the porous sphere are 10%–20% lower than that for an impermeable sphere which is consistent with the numerical simulation results of 2017 Wittig [3] which has the similar surface property with our porous sphere for the same sub-particle array mode. The good agreement between our C_D experimental results and the literature can further very the feasibility of the prepared spheres.

However, Masliyah and Polikar [4] found at higher Re, a porous sphere could experience a higher drag coefficient than that for an impermeable sphere with a same Re, see Fig. 13. The deviation may be due to the surface roughness of the porous sphere used in the

experimental study of 1980 Masliyah with sharp edges and fibre endings in the surface. And the interface between the porous sphere and fluid due to the different surface roughness may affect the drag acted on the porous sphere, which corresponded to the jump parameters used in numerical simulations and are called the "semi-slip" boundary condition. So, the computed result of 2012 Yu [2] is also smaller than that in 1980 Masliyah which is attributed to the different porous–fluid interface condition depended on the surface roughness properties and he verified the values of the jump parameters used might affect the drag acted on the surface of the porous sphere. Besides, the numerical simulation of Nandakumar and Masliyah [8] also indicates that at a higher *Re* range, the computed drag coefficients are about 10% lower than the experimental values of Masliyah and Polikar [4] due to the different surface property. Besides, the numerical simulation result of 2012 Jain [15] shows a peculiar phenomenon that the C_D of the porous sphere in the intermediate range of permeability and Reynolds number is greater than that of the impermeable sphere which also means drag ratio Ω being >1 and he thought this may be attributed to the formation of circulating cells and the back flow inside the porous permeable sphere based on different internal pore structures. The above "semi-slip" boundary condition for the porous–fluid interface and the different internal flow based on different internal pore structures can cause a difference on drag force due to the change of flow structure which will be studied in our next step combined with the flow field obtained from PIV (Particle Image Velocimetry) experiments for the model porous particles.

In summary, our results show that the drag coefficient of a homogenous porous sphere tends to be consistent with than of the impermeable spheres with the same *Re* in a low *Re* regime and it experiences a lower drag coefficient than that for an impermeable sphere at a higher *Re* regime which agrees well with the results in the literature indicating the feasibility of the prepared spheres. And the correlation for drag coefficients of porous spheres in a wider range of Reynolds numbers and normalized sphere radius β as well as the further research on the interaction between the porous particles and the surrounding fluid will be done in our next work.

4. Conclusion

The difficulty in preparation of porous spheres is a major impediment to the experimental research of porous particles due to their poor repeatability with the uncontrollability of pore structure as well as the non-homogeneity and the poor sphericity with the sharp edges and fiber endings exist [4,17,18]. This paper discussed a new method to construct porous spheres for a homogeneous porosity and homogeneous surface properties with a good sphericity for a wider range of permeability β. The detailed preparation process included coloring, binding and curing. The change of the mass ratio before and after coloring was controlled below 0.8% for all porous spheres. And the mass ratio of the binders in the porous sphere was lower than 1.9%, by which the effect of binders on the pore structure was minimized. Besides, with such low quantity of binders, it could still withstand rigid collisions at the maximum terminal velocity of 1 m/s and keep the structure intact.

PTV experiments with the prepared porous spheres were carried out to evaluate the feasibility of the use of these prepared model porous spheres via the measurement of terminal velocities in the gravity-driven settling experiments. The drag coefficients as well as the wall correction factor *K* of our prepared porous spheres fit well with the results in the literature which can certify our model porous spheres can be used for the experimental research of porous particles. A good reproducibility (The standard deviations were below 0.2%) for the same experimental conditions was achieved, owing to the homogeneous porosity and homogeneous surface properties.

We will then systematically study the interaction between porous particles and the surrounding fluid and the preparation and the feasibility evaluation of model porous spheres are the first step in our series of work. The porous spheres prepared via this new method are expected to play an important part in the experimental researches related to the flow of porous particles and could stimulate new studies to expose the unveiled phenomena and answer the unsolved questions related to the interaction between the porous particles and the surrounding fluid.

Acknowledgments

This work is part of a research program financially supported by the National Natural Science Foundation of China under Grant No. 91834302.

Nomenclature

Roman letters

C_D	drag coefficient, dimensionless
d	diameter of a sphere, mm
Da	Darcy number, dimensionless
d_p	diameter of monomers, mm
D	dimensions of the vessel, mm
F_b	buoyancy of the sphere, N
F_d	drag force, N
g	gravitational acceleration, m/s^2
G	gravity of the sphere, N
k	permeability of porous sphere, m^2
K	wall correction factor, dimensionless
k/d^2	permeability ratio, dimensionless
n	number of monomer in an aggregate, dimensionless
R	radius of the porous sphere
Re	Reynolds number, dimensionless
Re_t	particle Reynolds number for the terminal state, dimensionless
R_{rela}	correlation coefficient of polynomial fitting
S''	the surface ratio of the porous sphere compared to a solid sphere, dimensionless
T	temperature, °C
t	time, s
u_t	terminal velocity of the sphere, m/s
$u_{t,p}$	terminal velocity of the porous sphere, m/s
$u_{t,im}$	terminal velocity of the impermeable sphere with a same bulk density included fluid as the porous sphere, m/s
V_f	the volume of the fluid within the porous spheres, m^3
V_p	the volume of the solid skeletal part within the porous spheres, m^3

Greek letters

β	dimensionless radius of a sphere, dimensionless
ε	porosity of sphere, dimensionless
μ	dynamic viscosity of fluid, Pa·s
ρ_{bulk}	the bulk density of the porous sphere included the fluid inside the porous sphere, kg/m^3
ρ_f	the density of the fluid, kg/m^3
ρ_p	the skeletal density of the particle, kg/m^3
Ω	correction factor, dimensionless

Subscripts

p	particle
l	liquid

Abbreviations

PTV	particle tracking velocimetry

References

[1] C. Li, M. Ye, Z. Liu, On the rotation of a circular porous particle in 2D simple shear flow with fluid inertia, J. Fluid Mech. 808 (2016) R3.

[2] P. Yu, Y. Zeng, T.S. Lee, X.B. Chen, H.T. Low, Numerical simulation on steady flow around and through a porous sphere, Int. J. Heat Fluid Flow 36 (2012) 142–152.

[3] K. Wittig, P. Nikrityuk, A. Richter, Drag coefficient and Nusselt number for porous particles under laminar flow conditions, Int. J. Heat Mass Transf. 112 (2017) 1005–1016.

[4] J.H. Masliyah, M. Polikar, Terminal velocity of porous spheres, Can. J. Chem. Eng. 58 (1980) 299–302.

[5] Q. Guo, S. Meng, Y. Zhao, L. Ma, D. Wang, M. Ye, W. Yang, Z. Liu, Experimental verification of solid-like and fluid-like states in the homogeneous fluidization regime of geldart a particles, Ind. Eng. Chem. Res. 57 (2018) 2670–2686.

[6] D.D. Joseph, L.N. Tao, The effect of permeability on the slow motion of a porous sphere in a viscous liquid, Z. Angew. Math. Mech. 44 (1964) 361–364.

[7] G. Neale, N. Epstein, W. Nader, Creeping flow relative to permeable spheres, Chem. Eng. Sci. 28 (1973) 1865–1874.

[8] K. Nandakumar, J.H. Masliyah, Laminar flow past a permeable sphere, Can. J. Chem. Eng. 60 (1982) 202–211.

[9] B.S. Padmavathi, T. Amaranath, S.D. Nigam, Stokes flow past a porous sphere using Brinkman's model, Z. Angew. Math. Phys. 44 (1993) 929–939.

[10] P. Vainshtein, M. Shapiro, C. Gutfinger, Creeping flow past and within a permeable spheroid, Int. J. Multiph. Flow 28 (2002) 1945–1963.

[11] P.D. Verma, N.C. Sacheti, Low-Reynolds-number flow of a second-order fluid past a porous sphere, J. Appl. Phys. 46 (1975) 2065–2069.

[12] A.C. Srivastava, N. Srivastava, Flow past a porous sphere at small Reynolds number, Z. Angew. Math. Phys. 56 (2005) 821–835.

[13] N. Srivastava, Flow of a viscous fluid past a heterogeneous porous sphere at low Reynolds numbers, J. Appl. Mech. Tech. Phys. 57 (2017) 1022–1030.

[14] R.M. Wu, D.J. Lee, Highly porous sphere moving through centerline of circular tube filled with Newtonian fluid, Chem. Eng. Sci. 54 (1999) 5717–5722.

[15] A.K. Jain, S. Basu, Flow past a porous permeable sphere: hydrodynamics and heat-transfer studies, Ind. Eng. Chem. Res. 51 (2011) 2170–2178.

[16] K. Wittig, A. Golia, P.A. Nikrityuk, 3D numerical study on the influence of particle porosity on heat and fluid flow, Prog. Comput. Fluid Dyn. An. Int. J. 12 (2012).

[17] K.S. Matsumoto, A, Settling velocity of a permeable model floc, Chem. Eng. Sci. 32 (1977) 445–447.

[18] A. Emadzadeh, Y.M. Chiew, Settling velocity of a porous sphere, River Flow 2016 (2016) 555–562.

[19] F. Gruy, P. Cugniet, Experimental study of small aggregate settling, J. Colloid Interface Sci. 272 (2004) 465–471.

[20] R. Ge, M. Ghadiri, T. Bonakdar, K. Hapgood, 3D printed agglomerates for granule breakage tests, Powder Technol. 306 (2017) 103–112.

[21] P.P. Brown, D.F. Lawler, Sphere drag and settling velocity revisited, J. Environ. Eng. 129 (2003) 222–231.

[22] N.-S. Cheng, Comparison of formulas for drag coefficient and settling velocity of spherical particles, Powder Technol. 189 (2009) 395–398.

[23] A. Terfous, A. Hazzab, A. Ghenaim, Predicting the drag coefficient and settling velocity of spherical particles, Powder Technol. 239 (2013) 12–20.